



In Situ Observation of Rock Spalling in the Deep Tunnels of the China Jinping Underground Laboratory (2400 m Depth)

Xia-Ting Feng¹ · Hong Xu¹ · Shi-Li Qiu² · Shao-Jun Li² · Cheng-Xiang Yang¹ · Hao-Sen Guo¹ · Yuan Cheng² · Yao-Hui Gao²

Received: 4 May 2017 / Accepted: 16 December 2017 / Published online: 3 January 2018
© Springer-Verlag GmbH Austria, part of Springer Nature 2018

Abstract

To study rock spalling in deep tunnels at China Jinping Underground Laboratory Phase II (CJPL-II), photogrammetry method and digital borehole camera were used to quantify key features of rock spalling including orientation, thickness of slabs and the depth of spalling. The failure mechanism was analysed through scanning electron microscope and numerical simulation based on FLAC^{3D}. Observation results clearly showed the process of rock spalling failure: a typical spalling pattern around D-shaped tunnels after top-heading and bottom bench were discovered. The orientation and thickness of the slabs were obtained. The slabs were parallel to the excavated surfaces of the tunnel and were related to the shape of the tunnel surface and orientation of the principal stress. The slabs were alternately thick and thin, and they gradually increased in thickness from the sidewall inwards. The form and mechanism of spalling at different locations in the tunnels, as influenced by stress state and excavation, were analysed. The result of this study was helpful to those rethinking the engineering design, including the excavation and support of tunnels, or caverns, at high risk of spalling.

Keywords Spalling · Jinping Underground Laboratory · Marble tunnel · Photogrammetry · Quantitative characteristics

1 Introduction

Spalling is a common failure mode seen during the excavation of deep hard rock tunnels under high-stress conditions (Fairhurst and Cook 1966). A lot of work has been done to observe rock spalling behaviour in deep tunnels under high in situ stress. Hoek and Brown (1980) observed “V”-shaped rock spalling in a triangular tunnel and investigated various failure mechanisms along maximum tangential stress contours. Martin and Read (1996) and Martin et al. (1997) obtained the stress threshold at which spalling failure occurs and proposed an empirical formula for the relationship between the depth of spalling, stress, and rock strength according to the statistical analysis of spalling

failures in several underground laboratories constructed in hard rock. Ortlepp (1997) studied rock spalling associated with rockbursts in deep tunnels. Read (2004) investigated rock spalling in a circular mine at AECL and revealed the relationship between rock stress and spalling. Some research into the morphology and depth of spalling is available (Dowding and Andersson 1986; Diederichs 2007; Cai 2008; Martin and Christiansson 2009; Andersson et al. 2009; Lan et al. 2013; Qiu et al. 2014).

It is clear that many studies have promoted understanding of rock spalling. However, current studies on rock spalling mainly focus on small-scale tunnels and the quantitative characteristics of spalling in large deep tunnels at different excavation stages remains undefined. Huang et al. (2011) described the time of spalling as mainly occurring after several hours of excavation and recorded the thickness of slabs at the underground powerhouse of Jinping I hydro-power station (mainly in marble strata), China. The main shapes of spalling have been investigated through the in situ photo-observation at headrace tunnels with a 13 × 13 m section, Jinping II hydropower station, China (Feng and Hudson 2004, 2011; Wu et al. 2010, 2011; Hou et al. 2011; Feng et al. 2013).

✉ Xia-Ting Feng
xtfeng@whrsm.ac.cn; xia.ting.feng@gmail.com

¹ Key Laboratory of Ministry of Education on Safe Mining of Deep Metal Mines, Northeastern University, Shenyang 110819, China

² State Key Laboratory of Geomechanics and Geotechnical Engineering, Institute of Rock and Soil Mechanics, Chinese Academy of Sciences, Wuhan 430071, China

What are the characteristics of rock spalling in large D-shaped tunnels at great depth under top-heading and bottom bench, such as the distribution of thickness and number of slabs, orientation of slabs around sidewalls, and floors of the pilot tunnel, the evolution of rock spalling, and the depths of spalling in different locations? How is rock spalling affected by size and the sequence of excavation? What are the distribution shapes of slabs after rock spalling? What is time-dependent behaviour of rock spalling in marble tunnels? Therefore, the in situ observation of rock spalling has been conducted in D-shaped tunnels under the top-heading, slashing, and bottom bench of 7# and 8# Labs, China Jinping Underground Laboratory Phase II (CJPL-II). Photogrammetry, a digital borehole camera, and scanning electron microscopy (SEM) were used to characterise the individual slabs. Numerical simulation was conducted to understand

mechanism of rock spalling at D-shaped tunnels with top-heading, slashing and bottom bench excavation. This paper emphasises the characterisation of spalling in intact marble strata without macro-structural planes.

2 Geological and Engineering Information About the Test Site

Tunnels, 7# and 8#, at CJPL-II have a maximum overburden of 2400 m and are excavated in marble. Figure 1 shows the overall layout of the site. The strata around 7# and 8# Labs are mainly intact marble from the Baishan group (T_{2b}) of middle Triassic origin: the strata are more than 1.5 m in thickness with fine grains and have different colours including white marble, grey with white stripes, and black with

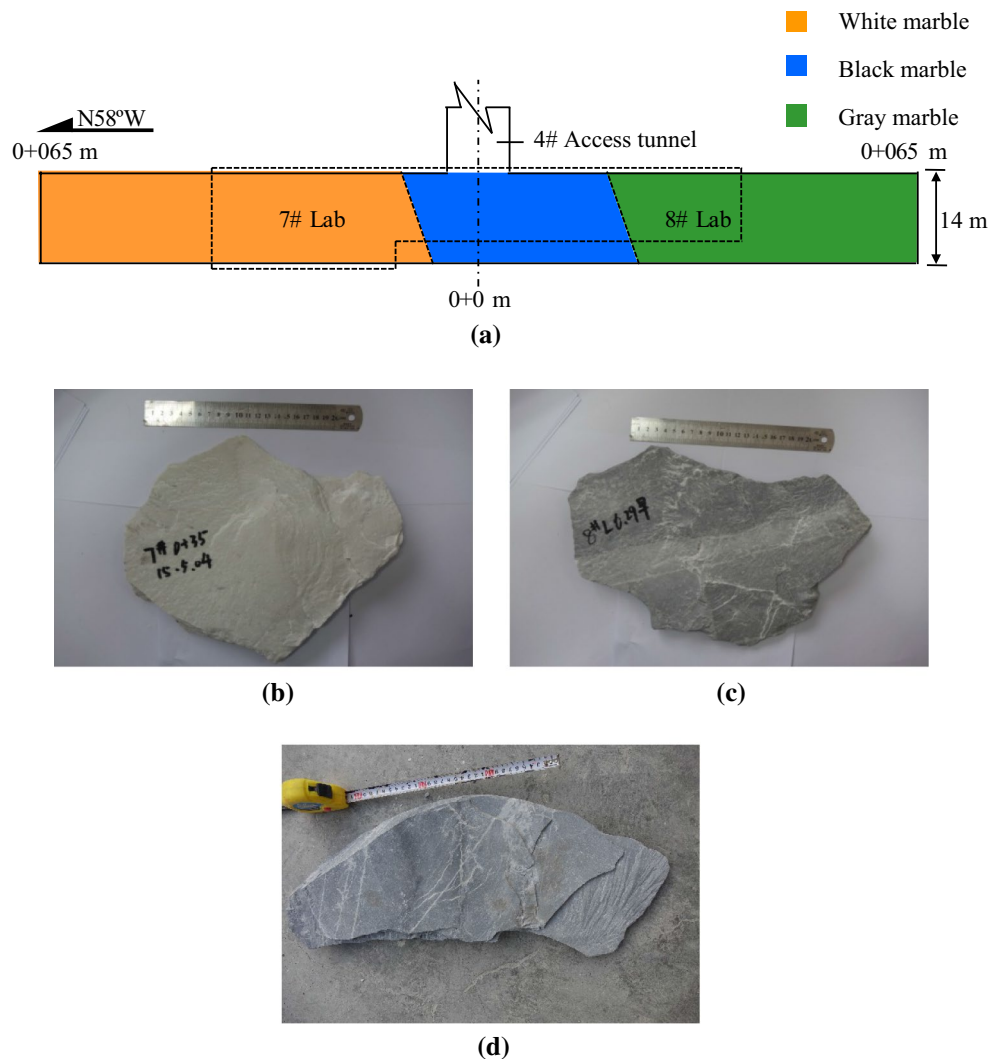


Fig. 1 Geological formation and lithology of 7# and 8# Labs at Jinping Underground Laboratory Phase II: **a** strata formation at 7# and 8# Labs, **b** white marble, **c** black marble and **d** grey marble. The zone

marked by dash line, without macro-structural planes, is used for investigation of rock spalling

white stripes. The dip angle of the bedding planes is 64° , and the dip direction of the bedding plane is $N94^\circ E$, which means the bedding plane intersects the tunnel axes with a big separative angle, as shown in Fig. 2. The main mineral composition of the rocks in different colours varies somewhat, consisting of dolomite and calcite, as shown in Table 1. A more detailed description of geological conditions can be found elsewhere (Feng et al. 2016).

The 7# and 8# Labs have a 65-m-long arcuate cross section measuring $14\text{ m} \times 14\text{ m}$. The axial direction of the laboratories lies on an azimuth of $N58^\circ W$. The centreline of the 4# access tunnel was regarded as chainage $0 + 000$, and then the chainage increases to the end of the laboratories on both sides at chainage $0 + 065$. A drilling and blasting method was used for excavation of the 7# and 8# Labs by two benches. The upper bench, with a height of 8.5 m, was excavated in two steps including the excavation of the top-heading (step I) and the slashing excavation of its sidewalls (step II) with a 3-m excavation footage. The bottom bench (step III) with 5.5 m high was advanced at 5.5 m per round, as shown in Fig. 3. The shotcrete (80 mm thick) was applied after excavation of the pilot tunnel. Rockbolts with diameter of 32 mm and 6.0 m in length were installed. Rockbolts at 1 m spacing plus steel mesh and shotcrete were installed after the slashing, and bench, excavations, respectively.

To observe the spalling in the surrounding rocks, boreholes were drilled in both sidewalls of each laboratory at chainage $0 + 035$ and chainage $0 + 045$ when the excavation

Table 1 Mineral composition of rock in 7# and 8# Labs

Rock samples	Dolomite (%)	Calcite (%)
White marble	87.10	12.90
Marble with white band	89.48	10.52
Grey marble	87.04	12.96
Black marble	88.13	11.87

of the pilot tunnel and slashing excavation were finished, respectively, to allow digital borehole camera measurement. The boreholes are located 1.5 m above the bottom of the pilot tunnel. Rock discing is illustrated in Fig. 4. Rock spalling at the working faces of the slashing excavation, II_a and II_b , can be seen (Fig. 5).

3 Measurement of Rock Spalling at Two Deep Tunnels

Two types of methods can be used to quantify the characteristic parameters of spalling (Gwynn 2013): one involves traditional contact measurements, such as compass and ruler measurements or borehole camera measurements, and the other involves non-contact measurement methods including laser scanning, photogrammetry (Feng et al. 2003; Pate and Haneberg 2011). Borehole camera measurements can be used to observe the fracture properties on sidewalls of

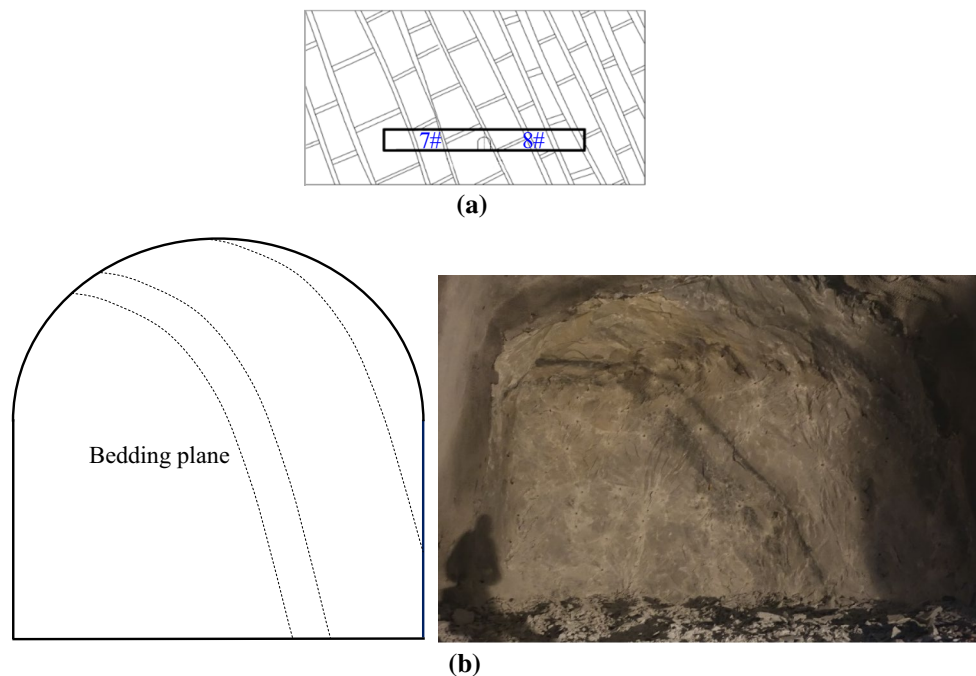


Fig. 2 Vertical geological cross section at China Jinping Underground Laboratory Phase II: **a** overall vertical geological cross section along the tunnel axis of 7# and 8# Labs and **b** longitudinal diagram: chainage $0 + 026$ of 7# Lab

Fig. 3 Excavation sequence and borehole layout in the 7# and 8# Labs. **a** Cross section and excavation zones of 7# and 8# Labs. Step I: top-heading, step II: side wall in the upper layer, step III: middle groove and side wall in the bottom bench. **b** Plan view and excavation direction of each zone for 7# and 8# Labs. T7-5, T7-6, T7-7, T7-8, T8-1, T8-2, T8-3, T8-4 are boreholes used for digital borehole camera testing. The direction of excavation was described in (b); step I was excavated firstly from the centreline of the 4# access tunnel to the end of each laboratory; step II began from the end of each laboratory to the centreline of the 4# access tunnel; II_a was the slashing excavation of the north-eastern side, and II_b was the slashing excavation of the south-western side; step III went from the centreline of the 4# access tunnel to the end of each laboratory

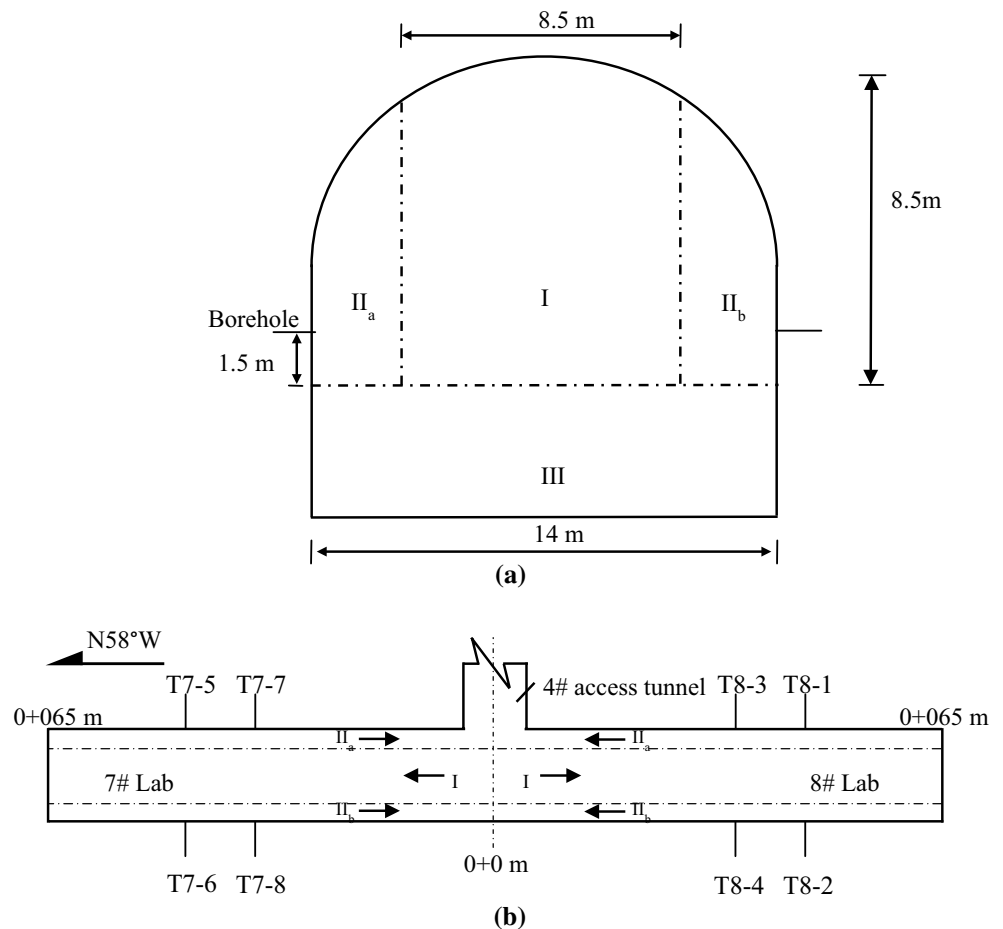


Fig. 4 Rock discing at borehole T8-2 in the south-western sidewall of 8# Lab, at chainage 0 + 045

boreholes (Li et al. 2013). The three-dimensional (3-d) laser scanning method can be adapted to observe slabs on the surfaces of the surrounding rock mass, but the orientation

of slabbed surfaces cannot be obtained directly from point cloud data. Additionally, point cloud data cannot be used to judge the surface condition directly.

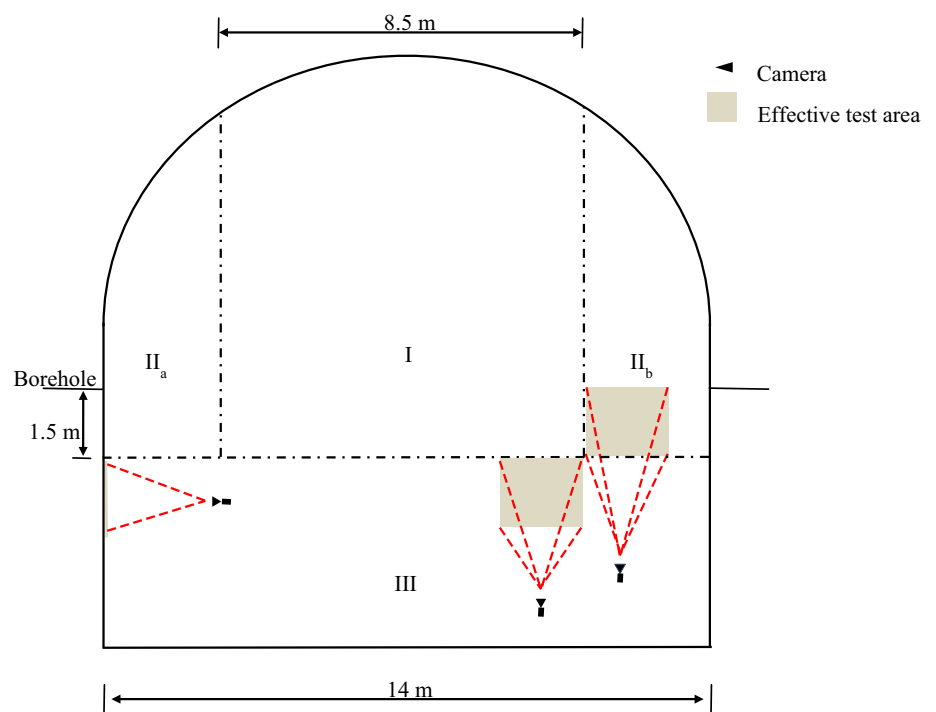
A photogrammetric method (Haneberg 2005; Pate and Haneberg 2011) was used to obtain a real 3-d model of the tunnel surface including the orientation, thickness, and depth of spalling (Fig. 6). A stereo camera system with D7100 single-lens reflex (SLR) was adopted to take images of the rock surfaces (Haneberg 2007). In general conditions, both of the test cameras can be used. Stereo cameras test at a high speed, while it is suggested that SLRs are employed to shoot targets beyond the test distance (3–11 m) of stereo cameras and in areas with high piles of debris and with lots of obstructions.

The data processing and analysis systems should be able to process 3-d images and analyse structures of rock masses, construct 3-d rock surface models using 2-d images, and determine 3-d geodetic coordinates of rock surfaces. The data from the left bank and right bank rock surfaces were combined, and the pixels in each image were matched by image processing software. Then the mosaicked images of rock surfaces were obtained after scaling, rotating, and translating the images. Based on the images of the rock surfaces,



Fig. 5 Rock spalling occurred after slashing excavation of II_b and II_a at the 7# Lab

Fig. 6 Arrangement of photogrammetric survey points at 7# and 8# Labs



3-d geological data were generated. Thereafter, spatial coordinates of each mosaicked 3-d image were calibrated by use of data obtained from the total station, so as to reconstruct the actual 3-d images. Finally, the orientations and thicknesses of the slabs were measured from 3-d images to form exportable statistical data.

4 Characteristics of the Rock Spalling in 7# and 8# Labs

Rock spalling at intact rock mass zone without macrostructural planes, marked by dash line in Fig. 1, has been observed and analysed.

4.1 Observation of Rock Spalling at the Sidewall of the Pilot Tunnel After Slashing Excavation

Figure 7 illustrates orientation of rock spalling observed at several typical working faces of intact rock mass zones. The results indicated that rock spalling mainly developed in the north-eastern sidewall of the pilot tunnel. By analysing the statistical distribution of slab surface orientations, it was concluded that: the inclinations of slabs approached 90°, and the surfaces of slabs intersected the sidewalls of the pilot tunnel at a shallow angle, lying approximately parallel to the sidewall of the pilot tunnel. However, the pattern of rock spalling at the floor corner of the pilot tunnel, where slab surfaces were turned to about 45°, is shown in Fig. 8.

Slab thickness was directly measured from the reconstructed 3-d model. Rock spalling of sidewalls of the pilot tunnel after slashing excavation is shown in Fig. 9, and the slabs of different thicknesses were measured from the

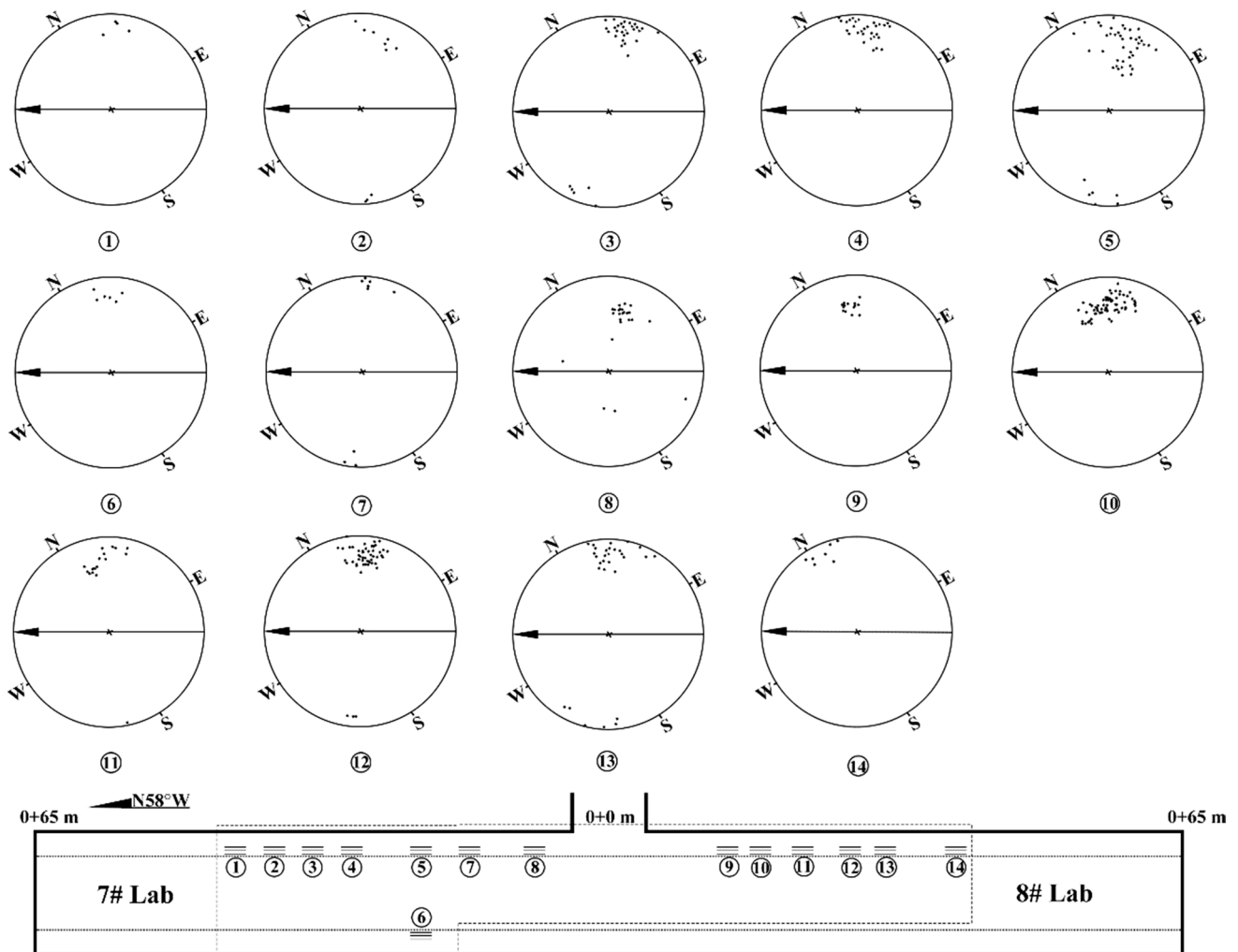


Fig. 7 Distribution of rock spalling orientations at typical working faces of slashing excavation (inside sidewalls of the pilot tunnel) in the intact rock masses. The arrow on the stereographic projection is the major axis of the laboratories under test

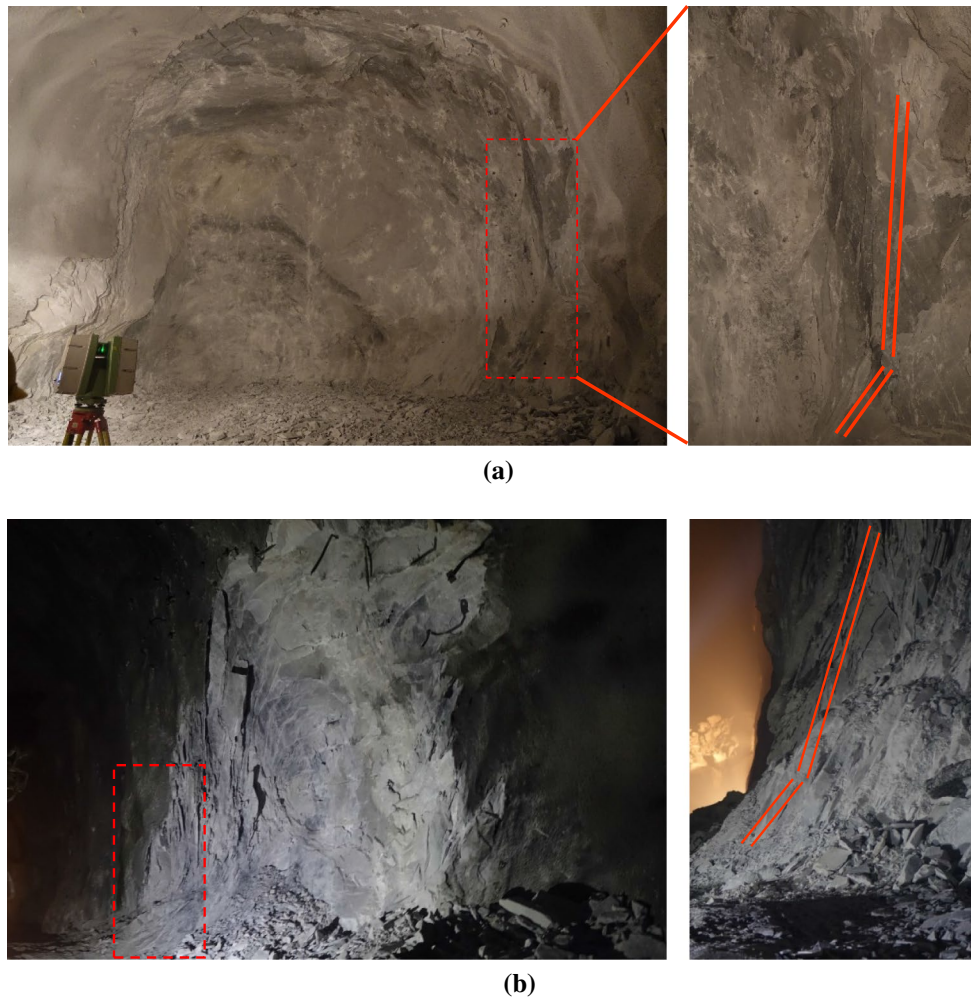


Fig. 8 **a** Rock spalling at north-eastern sidewall of the pilot tunnel of 7# Lab, at chainage 0 + 30. **b** Rock spalling of south-western sidewall of the pilot tunnel of 7# Lab at chainage 0 + 26 after excavation of the pilot tunnel

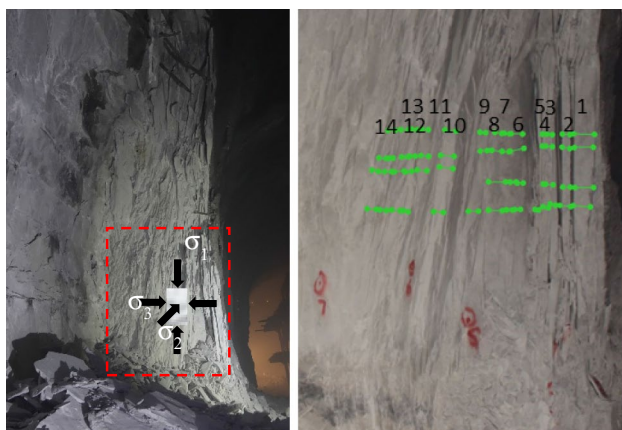


Fig. 9 Measurement of rock spalling at a typical working face of the slashing excavation

sidewall to the interior of the rock masses. The thickness of each slab at typical cross sections (Fig. 7) was measured. The minimum, maximum, and mean values are listed in Table 2. Figure 10 shows the thicknesses of slabs from the surface of the tunnel to the interior of the rock mass. The number and depth of slabs varying with location along the tunnel axis are shown in Fig. 11. The thickness of slabs gradually increased from the tunnel sidewall inwards. The slabs, moving from the sidewall inwards, were alternately thick and thin and gradually thickened rather than reaching a uniform thickness distribution. The number of slabs, maximum and minimum thickness of slabs, and depth of spalling at the north-eastern sidewall of the pilot tunnel of 8# Lab are smaller than those of 7# Lab.

Table 2 Layout of test points and the thickness of rock spalling as measured by photogrammetry

Test points	Lab no.	Chainage (m)	Maximum	Minimum	Average	Sidewall
①	7#	0 + 42	170	46	91.3	North-eastern
②	7#	0 + 38	140	46	85	North-eastern
③	7#	0 + 33.5	86	21	48.6	North-eastern
④	7#	0 + 29	112	27	56	North-eastern
⑤	7#	0 + 21	115	33	83.3	North-eastern
⑥	7#	0 + 21	115	25	65.1	South-western
⑦	7#	0 + 16	126	55	77.2	North-eastern
⑧	7#	0 + 8.5	140	70	109.9	North-eastern
⑨	8#	0 + 13.5	109	26	60	North-eastern
⑩	8#	0 + 17.5	85	38	59.5	North-eastern
⑪	8#	0 + 22	140	70	109.8	North-eastern
⑫	8#	0 + 27.5	109	51	74.9	North-eastern
⑬	8#	0 + 31.5	112	18	53.6	North-eastern
⑭	8#	0 + 39	100	31	53.7	North-eastern

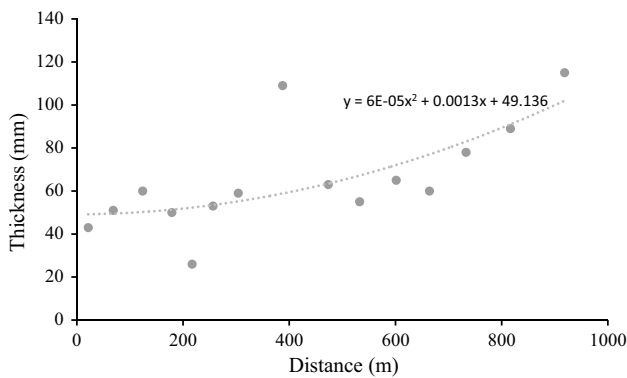


Fig. 10 Thickness distribution of slabs at 7# Lab observed after the slashing excavation

4.2 Observation of Rock Spalling at the Final Tunnel Sidewall

Several boreholes were drilled on sidewalls of final tunnel (Fig. 3), to research rock spalling around the final sidewall tunnel. The digital borehole camera results indicated that rock slabs are almost parallel to the sidewall, some of them having small changes in orientation (Fig. 12). However, the number of slabs and depth of rock spalling varied with location (Table 3), and the thicknesses of the slabs generally increased from the tunnel surface to the interior of the rock mass (Fig. 13). It can be seen that depth of spalling is about 0.9, 0.8, 1.0, 0.9, and 0.5 m in boreholes T7-5, T7-6, T7-7, T8-1, and T8-3, respectively. Rock spalling in boreholes T7-6, T7-7, and T8-1 is the most developed. The spalling strike in the sidewall of tunnel occurred parallel to the tunnel axis. Moreover, the slabs are alternately thick and thin and gradually thickened towards the interior of the surrounding

Fig. 11 Number of slabs and depth of rock spalling at typical north-eastern sidewall section of the pilot tunnels at 7# and 8# Labs along the direction of the tunnel axis

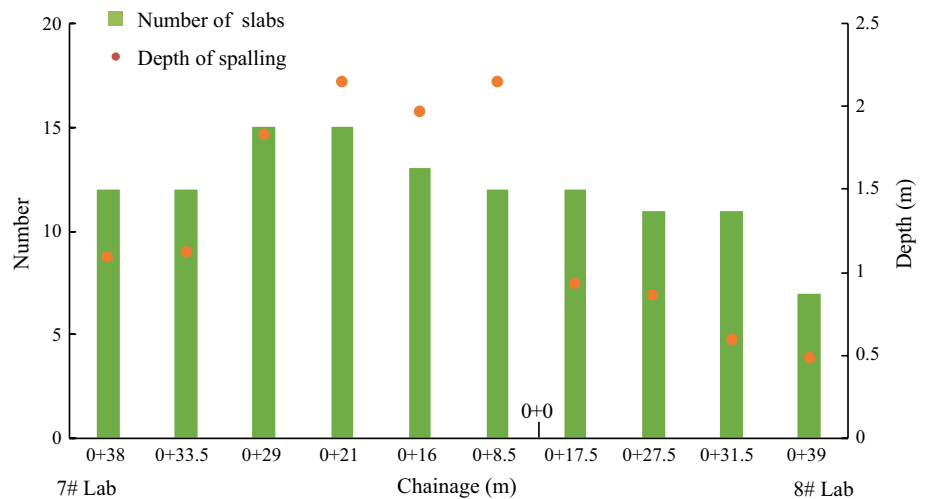


Fig. 12 Digital borehole camera images for different boreholes at final sidewalls of 7# and 8# Labs. The orientations of rock slabs are nearly parallel to final tunnel sidewall. L is the thickness of the rock slabs. The depths of spalling are about 0.9, 0.8, 1.0, 0.9, and 0.5 m at boreholes T7-5, T7-6, T7-7, T8-1, and T8-3, respectively. Rock spalling at boreholes T7-6, T7-7, T8-1 is the most developed

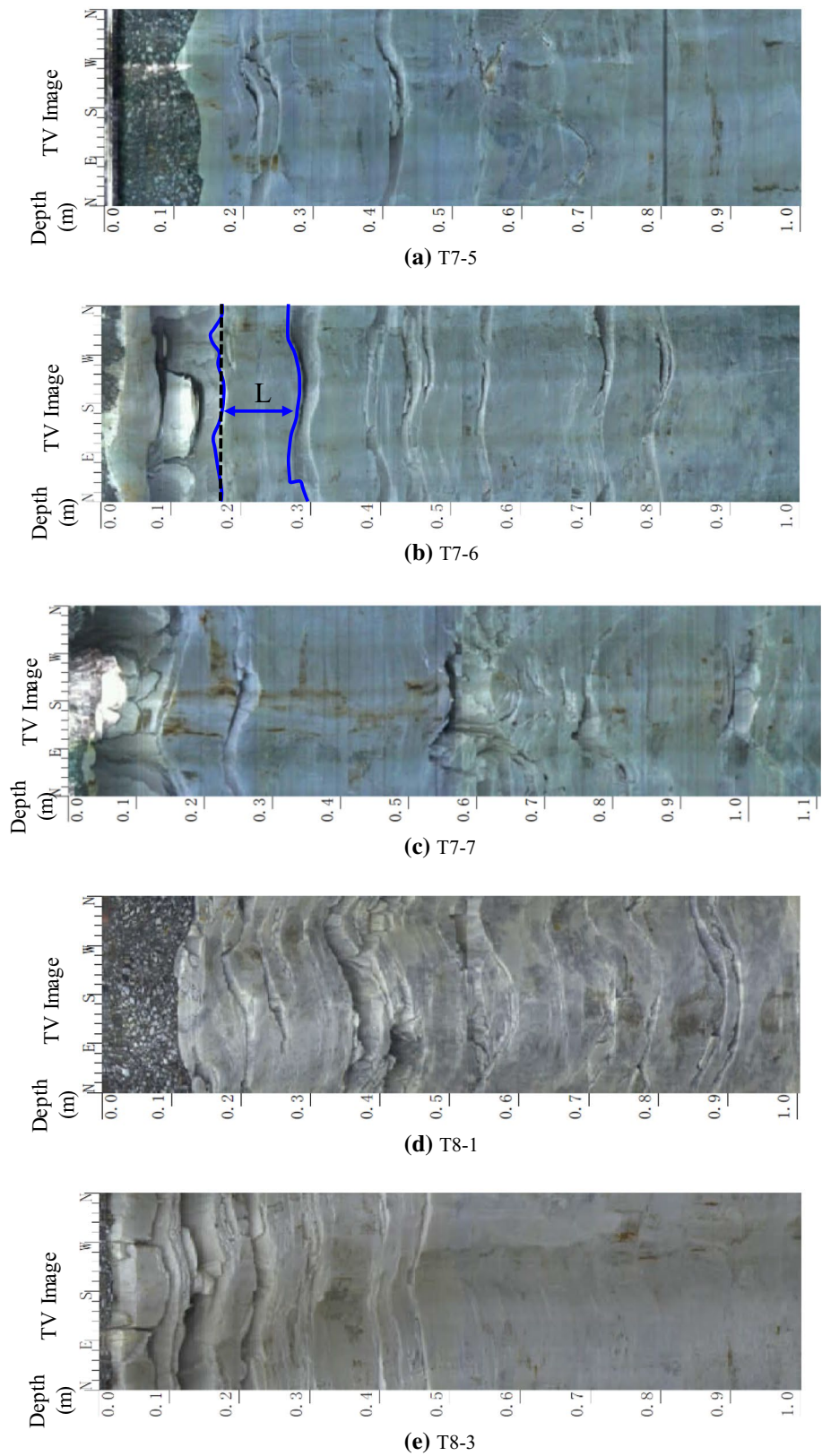


Table 3 Layout of boreholes and the thickness of spalling measured by digital borehole camera

Borehole no.	Lab no.	Length (m)	Chainage (m)	Max (mm)	Min (mm)	Ave (mm)	Depth (m)
T8-1	8#	6	0 + 45	267.3	14.3	91.5	1.67
T8-2	8#	6	0 + 45	176.3	36.7	106.6	1.76
T8-3	8#	6	0 + 35	79.7	13.3	35.5	2.21
T8-4	8#	6	0 + 35	290	34	112	2.05
T7-5	7#	6	0 + 45	163.3	81	118.1	1.34
T7-6	7#	6	0 + 45	162.3	31.3	82.6	0.82
T7-7	7#	6	0 + 35	28	9.6	17.9	1.56
T7-8	7#	6	0 + 35	179	49	102	1.4

rock mass. This is similar to the trend recorded by the photogrammetric method.

4.3 Observation of Rock Spalling After Excavation of the Tunnel Bench

The orientations of slab surfaces at the working face at corner of the pilot tunnel and bottom bench and the working face of bottom bench are illustrated in Fig. 14. The inclination of spalling in the interior of the surrounding rocks at the floor corner of the pilot tunnel, exposed after the excavation of the bottom bench, was small. The pole diagrams in Fig. 14b show that the slab surfaces at the working face of the bottom bench excavation were almost horizontal. Generally, the orientation of slab surfaces exposed after slashing excavation of the sidewalls presented the same trend with that at the floor corner of the pilot tunnel exposed after the excavation of the bottom bench, and the dip angle of such slabs significantly decreased in the floor corner of the pilot tunnel. This indicated that the spalling orientation was related to the disposition of the tunnels.

The figures show the thickness of rock slabs generated around the south-western and north-eastern floor corner of the pilot tunnel after the excavation of the bottom bench (Fig. 15). The figure shows that the overall thickness of the

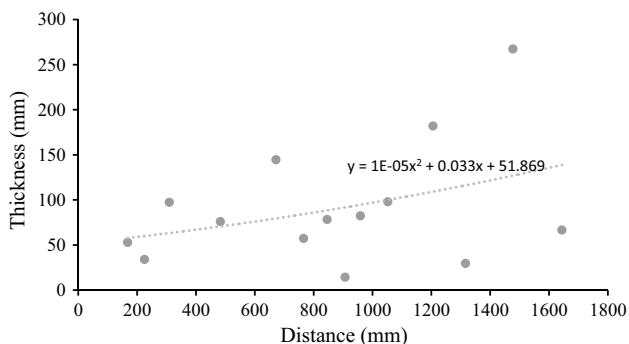


Fig. 13 Thickness of rock slabs at T8-1 borehole as seen by digital borehole camera. The distance indicates location from sidewall to inside rock mass at T8-1 borehole

slabs after the excavation of the bottom bench was slightly larger than that of slabs after the slashing excavation. The thickness of slabs was alternating between thick and thin from slashing excavation surfaces of sidewall to the interior of the surrounding rock masses. The slab thickness, in general, increased from the tunnel sidewall inwards.

The photograph taken from the borehole at the end of the bottom bench of the 7# Lab. indicated that there are several parallel cracks that propagated as a result of rock spalling from the sidewall (Fig. 16). The pattern of rock spalling at the sidewall of the pilot tunnel, in which the slabs at the middle are nearly parallel to the floor of the pilot tunnel, and pattern of rock spalling near the floor corner of the pilot tunnel, in which slab surfaces are turned to about 45°, are shown in Fig. 17, respectively.

By integrating Figs. 8, 12, and 17, the overall pattern of rock spalling observed after excavation of the pilot tunnel, slashing, and the bottom bench is shown in Fig. 18: it matched the principal stress direction predicted by numerical simulation (FLAC^{3D}) after the top-heading excavation based on in situ geo-stress test results (Fig. 18b).

4.4 Surface Characteristics of the Slabs

The shapes of fracture surfaces of slabs reflect the micro-crack characteristics (Pollard and Aydin 1988). The shapes of fracture surfaces observed in both tunnels are classified into four types, as shown in Fig. 19:

Type I Shell-shaped or feather-shaped concentric fracture surfaces (Fig. 19a). They have a flat centre and rib pattern distributed around the centre, forming an arcuate boundary line at the end of the rib patterns. The concentric feather pattern forms far away, even on the boundary of the slabs, in the rib patterns. The slabs are conchoidal on the whole.

Type II Flat shape (Fig. 19b). Slabs are straight and flat with linear patterns oriented in a certain direction.

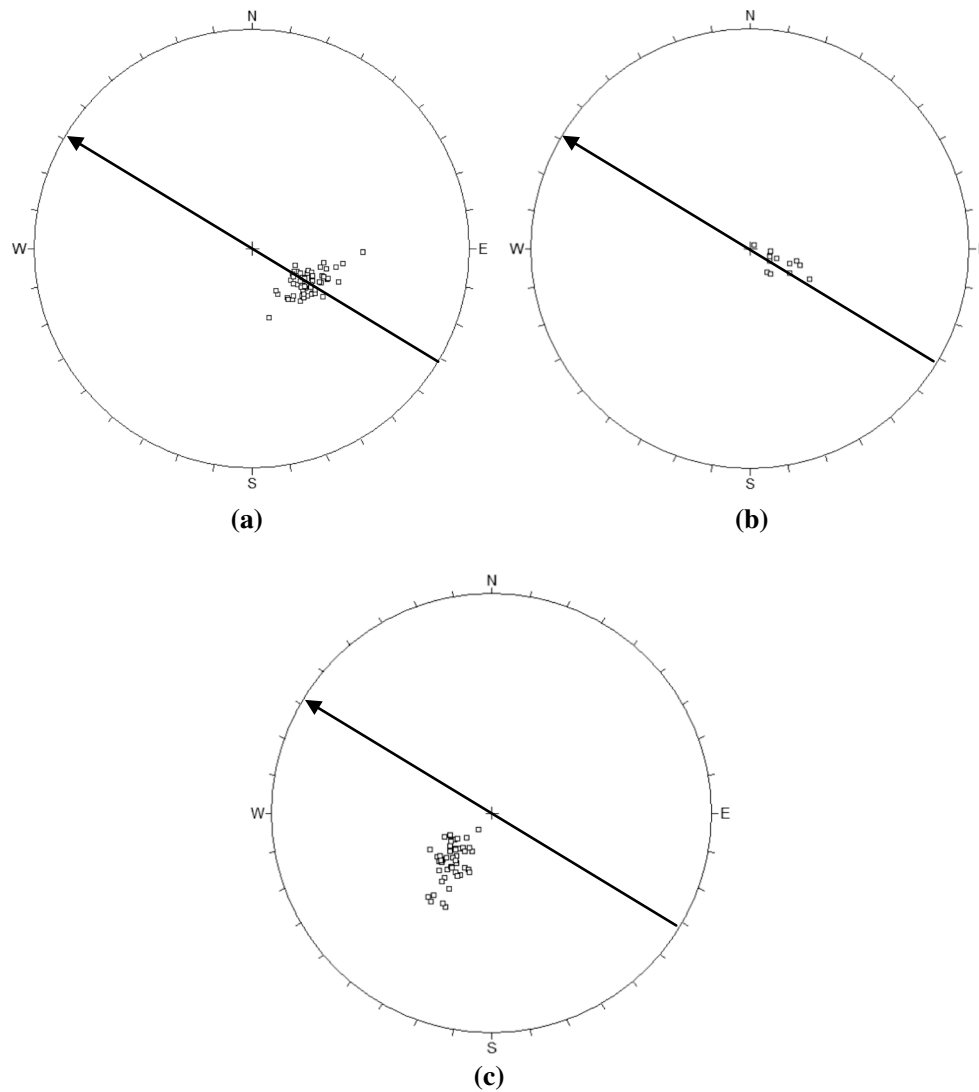


Fig. 14 Orientation of slab surfaces after excavation of the bottom bench at **a** the working face (chainage 0 + 037) near the north-eastern floor corner of the pilot tunnel, 8# Lab, **b** the working face (chainage

0 + 31) of the bottom bench, 8# Lab, and **c** the working face (chainage 0 + 32.5) near the south-western floor corner of the pilot tunnel, 7# Lab

- Type III Ripple shape (Fig. 19c). Slabs present rippled patterns from the centre to all around, thus having a similar pattern to that seen in the flat slabs.
- Type IV Combined shape in Fig. 19d. Slabs are large and comprised of several tight slabs; feather patterns are seen at the centre of each slab of different thickness.

4.5 Evolution of Rock Spalling

Comparing rock spalling observed on the day of excavation with that of the second day, cracks were open and the orientation of the rock slabs changed thereafter (Figs. 20, 21, for example). The results indicated that time-dependent

behaviour governed marble spalling due to high stress and ductile behaviour thereof at high stress.

5 Mechanism Analysis of Rock Spalling in 7# and 8# Labs

5.1 Influence of Geo-stress on Spalling Pattern

In situ stress measurement by over-coring near the end of 7# Lab indicated that the maximum, intermediate, and minimum principal stresses were about 70, 65, and 30 MPa, respectively. The maximum principal stress was inclined clockwise by 25° which results in the observed spalling pattern (Fig. 18). Actually, after excavation of the pilot tunnel,

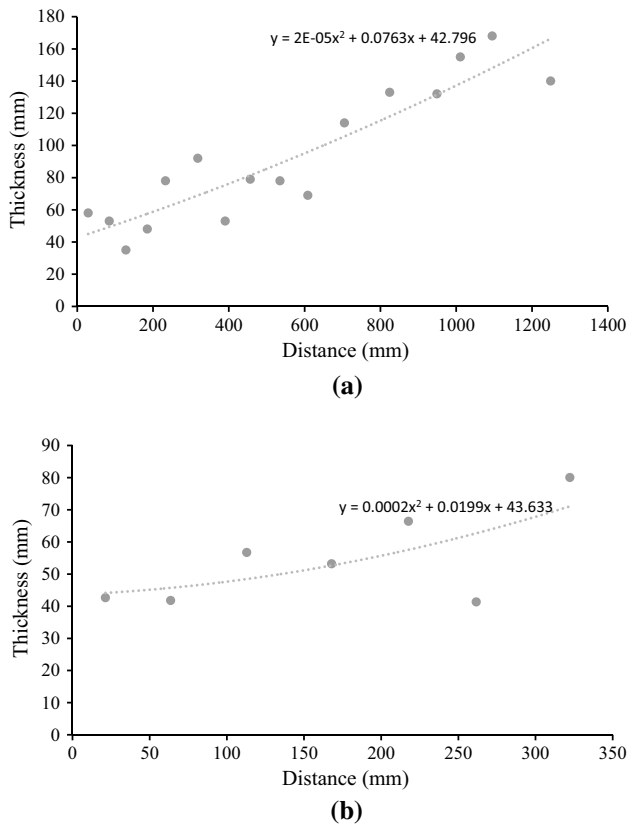


Fig. 15 Thickness of rock slabs after excavation of the bottom bench **a** south-western floor corner of the pilot tunnel of 7# Lab, chainage 0 + 032.5; **b** north-eastern floor corner of the pilot tunnel of 8# Lab, chainage 0 + 041. Distance measured from the sidewall of the excavation boundary to inside the rock mass and vertical to the rock slab surface

σ_3 at the surface of the sidewall decreased to zero. In addition, the strength of the rock mass was reduced and the area fractured in the region of stress concentration. The fracture was parallel to the tangential stress, so it could be seen that the spalling of these slabs was parallel to the sidewall of

the tunnel, and with the increase in depth, the direction of the tangential stress changed and the direction of slabs also changed (Fig. 18). The direction of the tangential stress followed the profile of the tunnel cross section, resulting in same changes in the orientation of the spalling. Cheon et al. (2011) verified this feature in model tests with holes. We simulated the stress distribution after pilot tunnel excavation in 7# and 8# Labs, and the adjusted stress directions are shown in Fig. 18b. There were different orientations of spalling seen at different locations: the orientation of spalling at the sidewall of the pilot tunnel observed after slashing excavation was parallel to the sidewall (Fig. 7), the orientation of spalling observed from the working faces of the bottom bench was parallel to the floor of the tunnel, and the orientation of spalling around the floor corners of pilot tunnel was about 45° (Fig. 14). As the orientation of the stresses determined the orientation of the slabs, most of the spalling occurred around the north-eastern sidewall and floor, with some in the south-western spandrel and side wall. It was difficult to detect any rock spalling at the south-western spandrel of the tunnel because it was not revealed by slashing excavation in most cases.

5.2 Influence of the Excavation

A numerical simulation, based on FLAC^{3D}, was carried out to simulate the excavation process of 7# and 8# Labs and thereof to investigate the effects of the chosen excavation method on spalling. The rock mass properties were back-analysed from multiple measurements including depth of excavation damage zone and displacement, using an intelligent back-analysis procedure (Feng 2000). The size of the model was $100 \times 100 \times 300 \text{ m}^3$. The geo-stress was obtained from the result of in situ stress measurement by over-coring. The constitutive model RDM (Jiang et al. 2008) for deep hard rock was used to describe the mechanical behaviour of surrounding rock. The failure approach index (FAI), which could determine the degree and location of the failure in

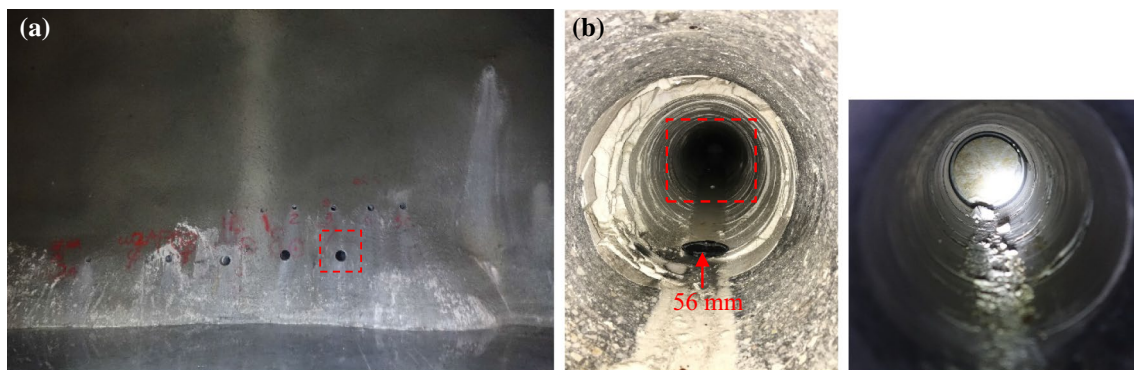


Fig. 16 **a** Boreholes and **b** nearly parallel cracks in the boreholes at the working face of the bottom bench of 7# Lab at chainage 0 + 65

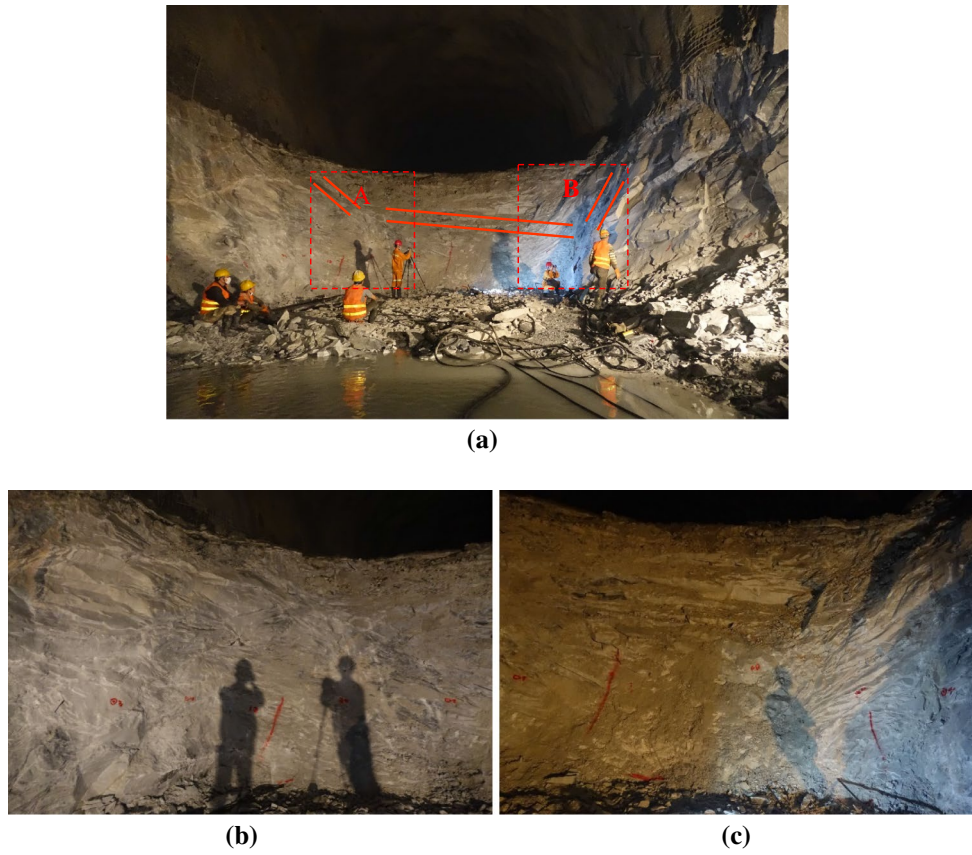


Fig. 17 **a** Rock spalling at working face of bench of 7# Lab at chainage 0 + 38. **b** Enlarged image of A in (a), **c** Enlarged image of B in (a)

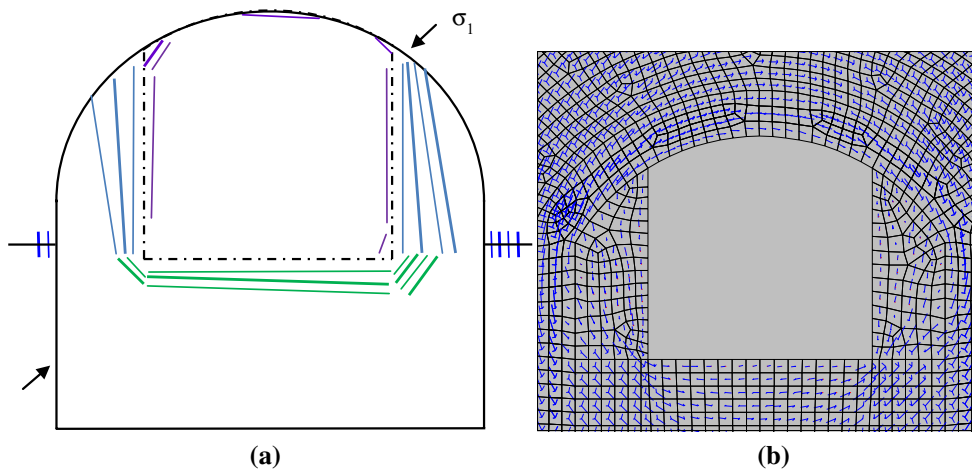


Fig. 18 **a** Typical pattern of rock spalling at 7# Lab (facing 7# Lab). The purple lines show the rock spalling pattern after excavation of the pilot tunnel. The wavy blue lines show rock spalling pattern at the slashing excavation working face. The green lines show rock spalling

pattern at working face of the bottom bench excavation. The blue lines show rock spalling at final tunnel sidewall observed at the borehole. **b** The principal stress orientations diagram after the excavation of pilot tunnel (colour figure online)

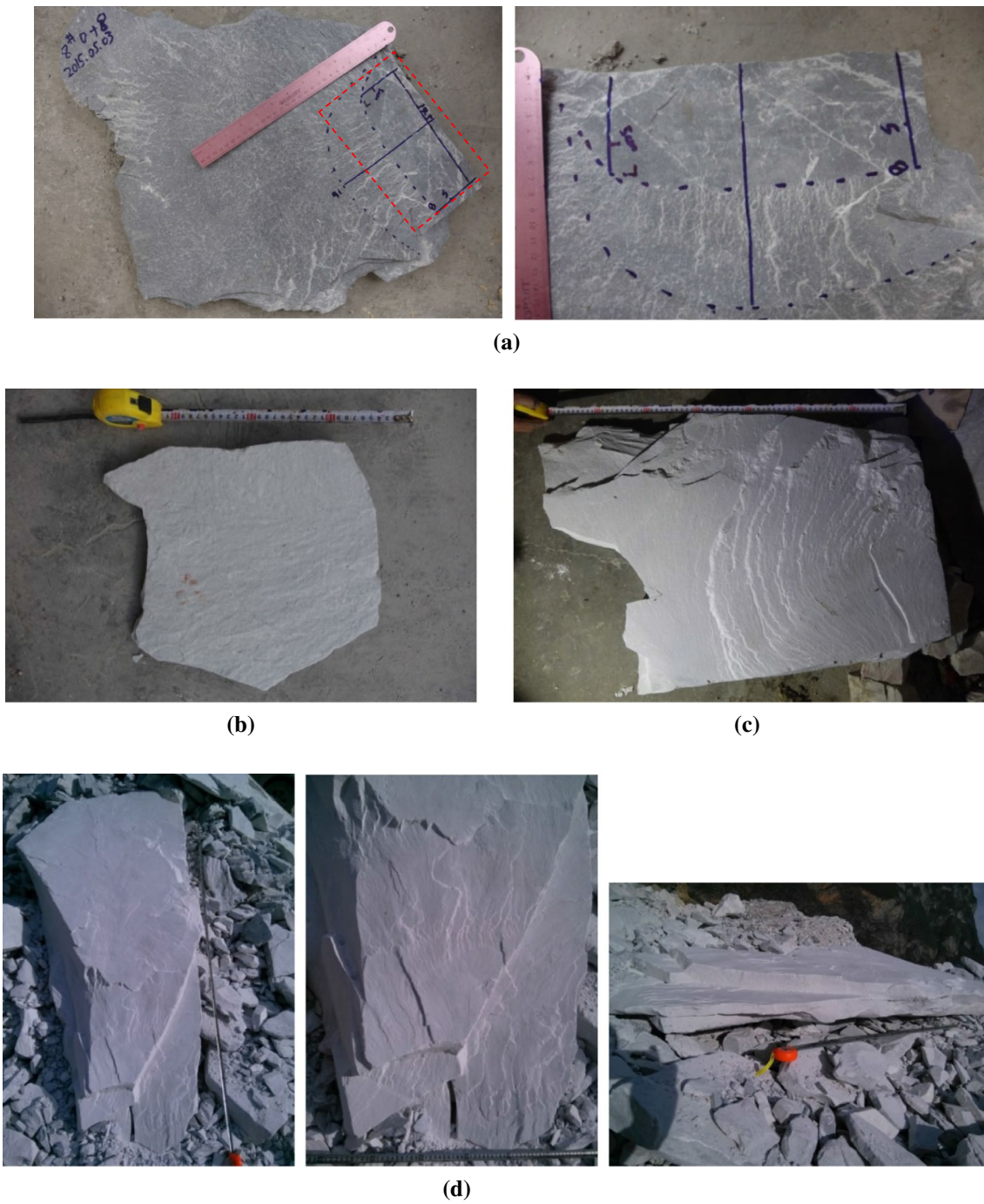


Fig. 19 Different types of fracture surfaces of slabs in intact marbles at 7# Lab and 8# Lab: **a** shell-shaped or feather-shaped concentric fracture surfaces, **b** flat fracture surfaces of a slab in two sides, **c** ripple-shaped fracture surface, and **d** combined-shape fracture surfaces

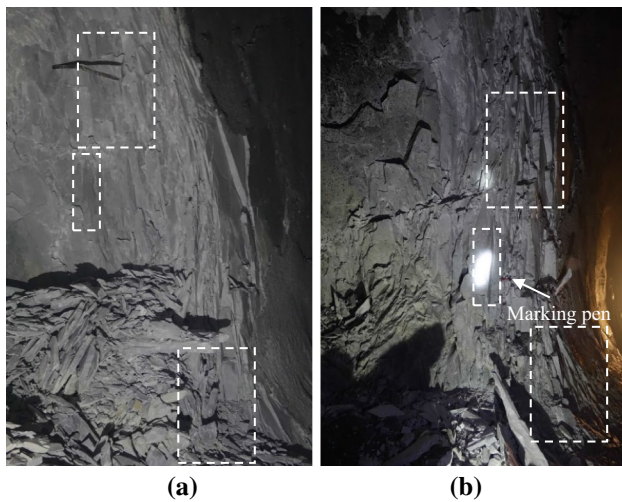


Fig. 20 Rock spalling at working face of the slashing excavation II_a (north-eastern sidewall of the pilot tunnel) of 7# Lab at chainage 0 + 33.5 observed **a** on the excavation day and **b** on the second day after excavation

surrounding rocks (Zhang et al. 2007), was used to evaluate the spalling. According to the definition of FAI, the range of $FAI \geq 1.0$ means excavation damage zone and failure zone, and this range can be considered as spalling in hard rock. The cross section at chainage 0 + 35 (7# Lab.) comprised the observation section.

The distribution of stress concentration after the pilot tunnel excavation, sidewall slashing excavation, and bench excavation is shown in Fig. 22. The stress concentration was mainly at north-eastern sidewall and floor, and some stress concentrations occurred at the south-western spandrel and

the side wall after the excavation. These were the positions where the rock spalling occurred in situ.

According to the evolution process of calculated FAI during excavation of the pilot tunnel shown in Fig. 23a–d, the range and depth of rock spalling increased significantly at first and then slowed down with the working face going away from the observation section, as shown in Fig. 23a–c where the distances between working face and observation section are 1, 5, and 10 m, respectively. When the working face was more than 10 m away, spalling almost stopped, compared to the range and depth of spalling after the pilot tunnel excavation was completed (Fig. 23d). Therefore, in a certain range, the closer to the 4# access tunnel, that means the farther the distance from working face which stood at the end of the labs after excavation of pilot tunnel, the deeper the spalling developed. And then spalling depth remains constant if the distance was large enough. This is consistent with the observed results shown in Fig. 11. The same process can also be obtained during the slashing excavation, as seen in Fig. 23e–g, except that the sensitive distance from working face was 5 m which was less than that during excavation of the pilot tunnel. Similar characteristics could be found in bench excavation as shown in Fig. 23h–j, and the sensitive distance from working face of bench excavation was 5 m. Comparing Fig. 23d with Fig. 23g, the depth of spalling after the pilot tunnel excavation was deeper than that after the sidewall slashing excavation. This is mainly because cross section of the pilot tunnel (8.5 m in width) was larger than that of the sidewall slashing excavation (2.75 m in width) and was subjected to more significant unloading and consequently deeper spalling. That was why the depth of rock spalling after the pilot tunnel excavation

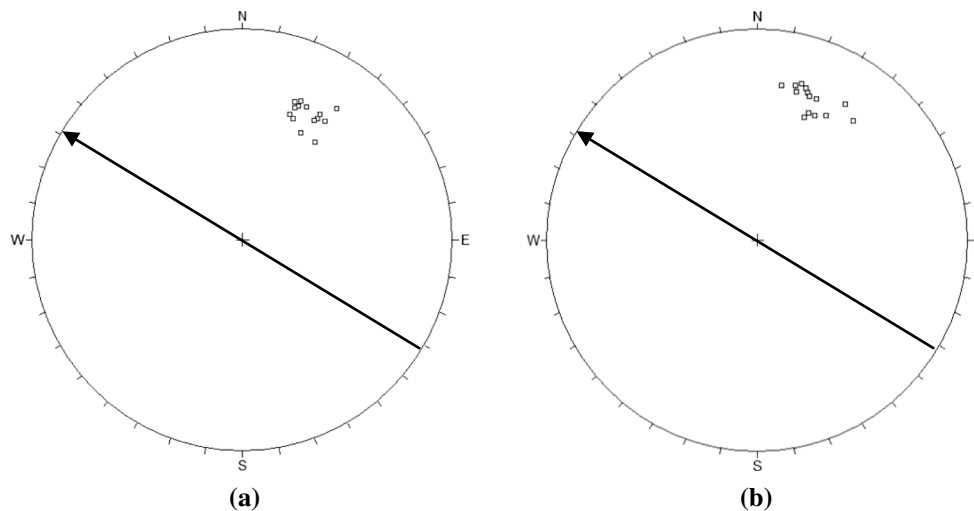


Fig. 21 Orientation of slabs at working face of slashing excavation (north-eastern sidewall of the pilot tunnel) of 8# Lab at chainage 0 + 14 observed **a** on the excavation day and **b** on the second day after excavation (obviously open and larger different angles of rock slabs)

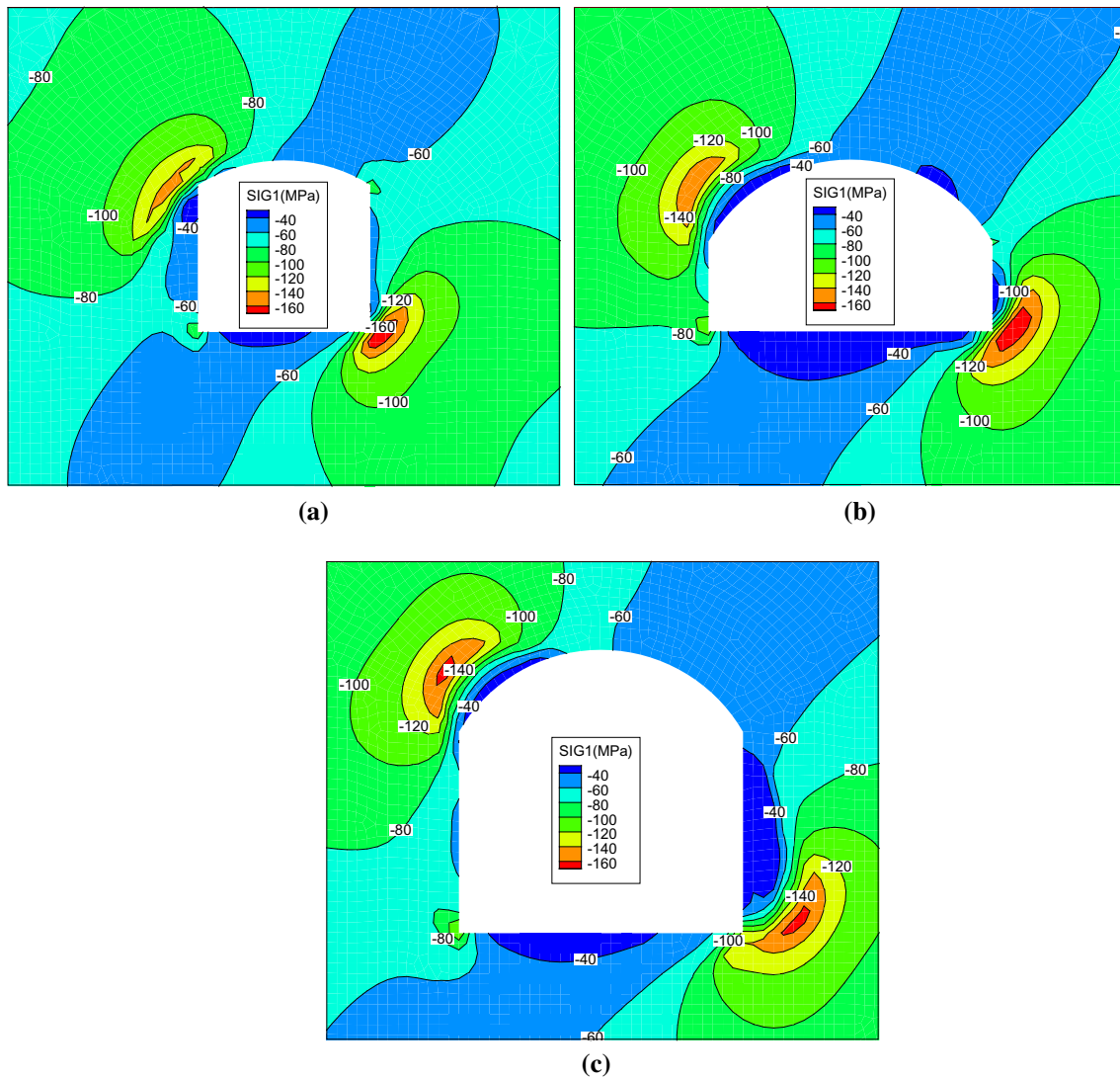


Fig. 22 Distribution of adjusted maximum principal stress at 7# Lab after **a** excavation of the pilot tunnel, **b** slashing excavation of the pilot tunnel, and **c** excavation of the bottom bench

(photogrammetric result, Fig. 4) was deeper than that after the slashing excavation (borehole camera result, Fig. 24a).

5.3 Meso-scale Fracture Mechanism Governing Spalling Behaviour

Slabs produced by in situ spalling were sampled, and SEM investigation was carried out. Typical micro-fracture images of slabs were acquired. Figure 25 shows the micrographs of slabs at the tunnel surface, Fig. 26 shows micrographs of the inner slabs of surrounding rock, and Fig. 27 shows micrographs of

slabs at the floor corner of the pilot tunnel. Figure 28 shows the SEM result for a rock sample without spalling but from the same place. By observing the three images of slabs magnified 100 times, the grain contours could be seen clearly. The overall fracture of slabs was generally found to take the form of intergranular fractures. By combining the images magnified 800 and 2000 times, it was found that the fracture of the specimens exhibited fluctuations in step-wise forms. It was obvious that intergranular and transgranular fractures increased in slabs compared with unstressed samples. The intergranular fractures were the dominant form of slabs, accompanied by a mixture

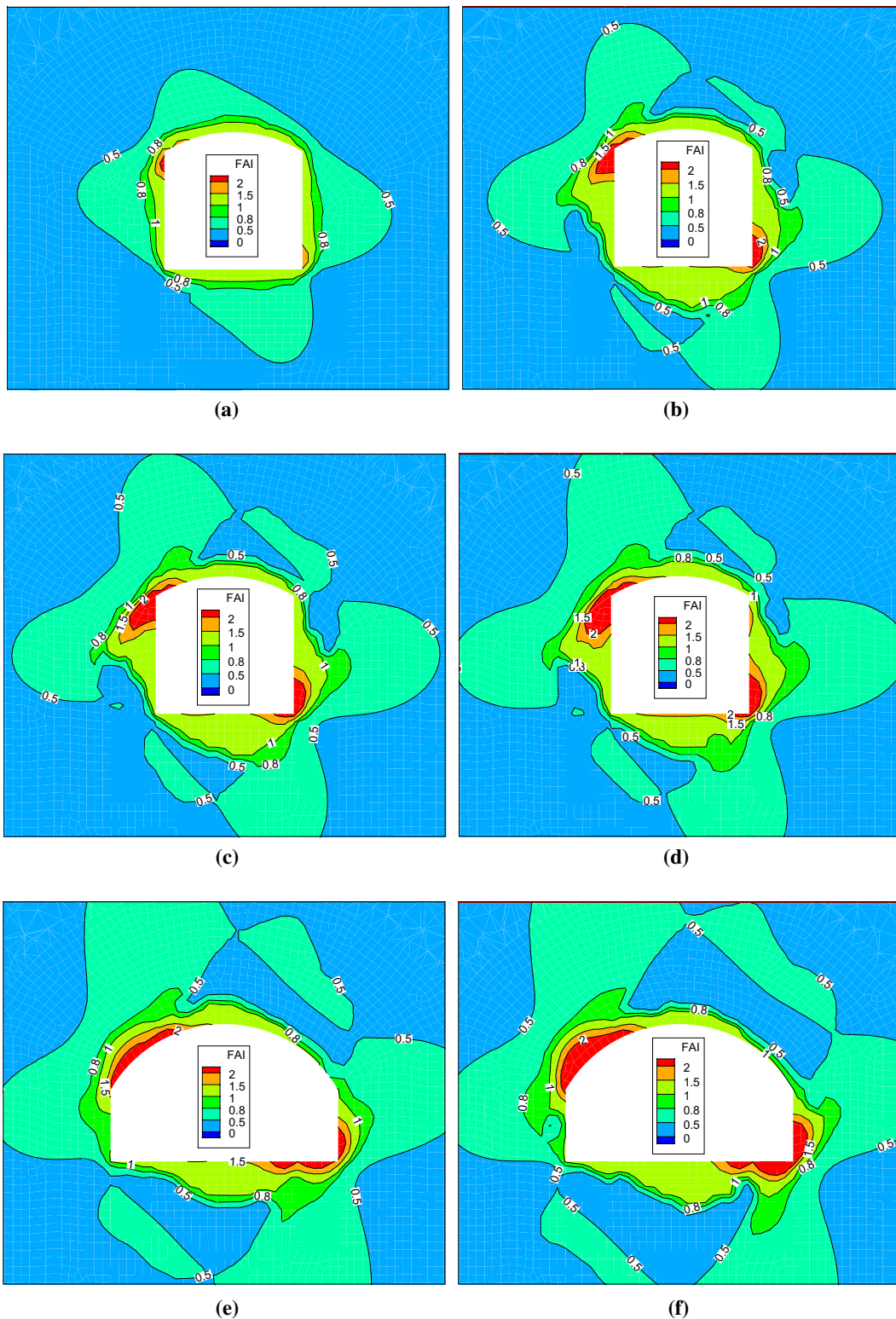


Fig. 23 Distribution of FAI in the surround rock of 7# Lab (The cross section at chainage 0 + 35 comprised the observation section) with **a** excavation working face of the pilot tunnel at chainage 0 + 036, **b** excavation working face of the pilot tunnel at chainage 0 + 040, **c** excavation working face of the pilot tunnel at chainage 0 + 045, **d** top-heading finished, **e** slashing excavation working face of the pilot

tunnel at chainage 0 + 034, **f** slashing excavation working face of the pilot tunnel at chainage 0 + 030, **g** slashing excavation finished, **h** excavation working face of the bottom bench at chainage 0 + 036, **i** excavation working face of the bottom bench at chainage 0 + 040, and **j** complete excavation of the bottom bench

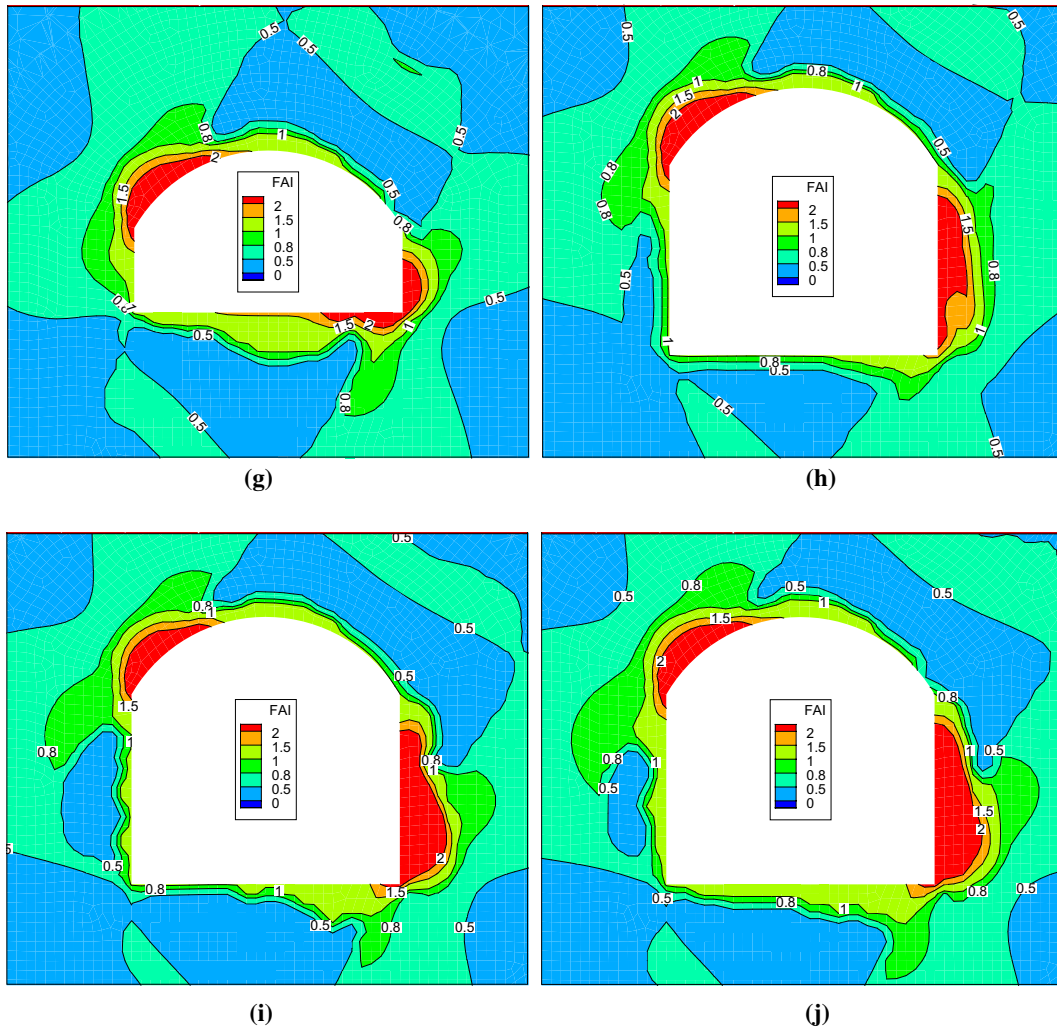


Fig. 23 (continued)

of intergranular and transgranular fractures. The micrographs also showed that the specimens had distinct edges and corners, smooth, flat, parallel side surfaces, which presented typical characteristics of tensile failure, because more brittle failures occurred at the tunnel surface and more ductile failures in the inner surrounding rock, there were more transgranular failures

seen in Fig. 25 and more intergranular failures seen in Fig. 26. The shear damage might have been caused by principal stress rotation (Eberhardt 2001), and we could see some parallel scratches in those slabs at the floor corner of the pilot tunnel (Fig. 27).

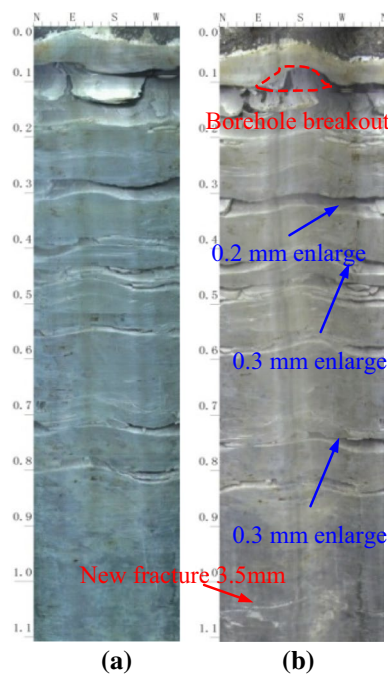


Fig. 24 Digital borehole camera images **a** after slashing excavation and **b** after the bottom bench excavation of T7-6

6 Conclusions

A photogrammetric measurement method, combined with a digital borehole camera method, has been used to study rock spalling in the deep D-shaped tunnels excavated in marble strata, the 7# Lab and 8# Lab of China Jinping Underground Laboratory Phase II. A 3-d model was built to measure the characteristics of rock slabs and the depth of spalling. The following conclusions may be drawn:

1. A typical spalling pattern around D-shaped tunnels under top-heading, slashing, and bottom bench excavation (Fig. 18), has been found.
2. All slab surfaces of intact rock masses in the 7# and 8# Labs were nearly parallel to the tunnel surface. As for the orientation, the surfaces of slabs extended along the direction of the excavation of the pilot tunnel and converged in the direction of the slashing excavation. The inclination of the slabs varied with location and was related to the orientation of geo-stress and tangential stress. The inclination of slabs at the sidewalls was almost vertical, while slabs at the floor corner of the pilot tunnel decreased to 45° angles and slabs at the tunnel floor turned to horizontal. The size and steps of excavation and the variation of the tunnel profile led to changes in the magnitude of unloading and differences in the direction of tangential stress (Fig. 18), and consequently the pattern of rock spalling.
3. The slabs were alternately thick and thin, and they gradually increased in thickness from the sidewall inwards.
4. Spalling in 7# and 8# Labs showed time-dependent behaviour under high stress. The longer the exposure time, the deeper the spalling (Fig. 11), and after excavation, the spalling still caused opening and extension of slabs to form new fractures (Fig. 21).
5. Spalling was dominated by tension, with shear failures arising in local areas. The spalling mechanism can mainly be explained by intergranular fractures, with a mixture of intergranular and transgranular fractures present. There were more transgranular fractures at tunnel surfaces undergoing brittle failure (Fig. 25) and more intergranular fractures at the inner surrounding rock (Fig. 26) upon ductile failure: shear failure may have occurred at the floor corner (Fig. 27).

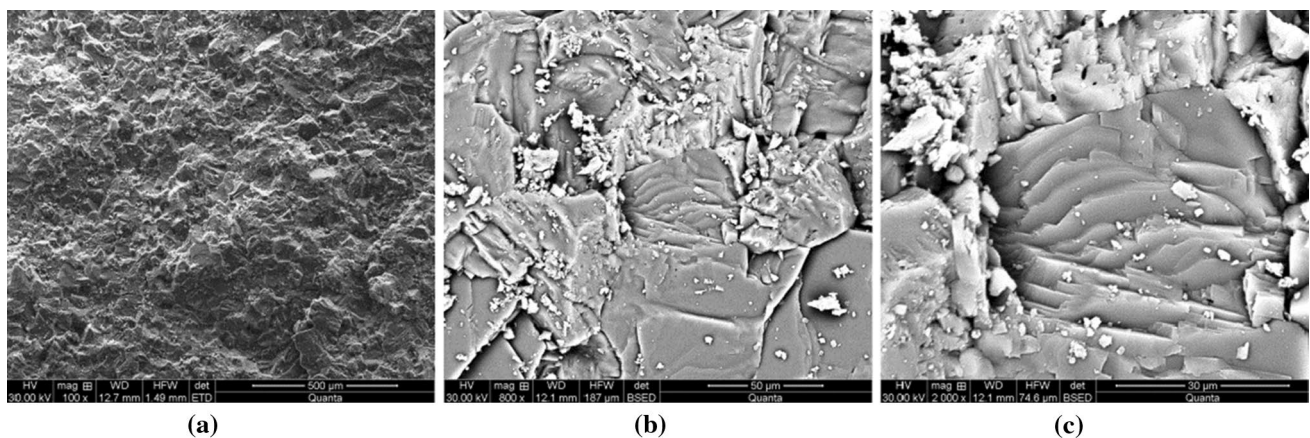


Fig. 25 Micrographs of slabs at the north-eastern sidewall tunnel surface of the pilot tunnel of 7# Lab at chainage 0 + 024. **a** Magnification ×100, **b** magnification ×800, **c** magnification ×2000

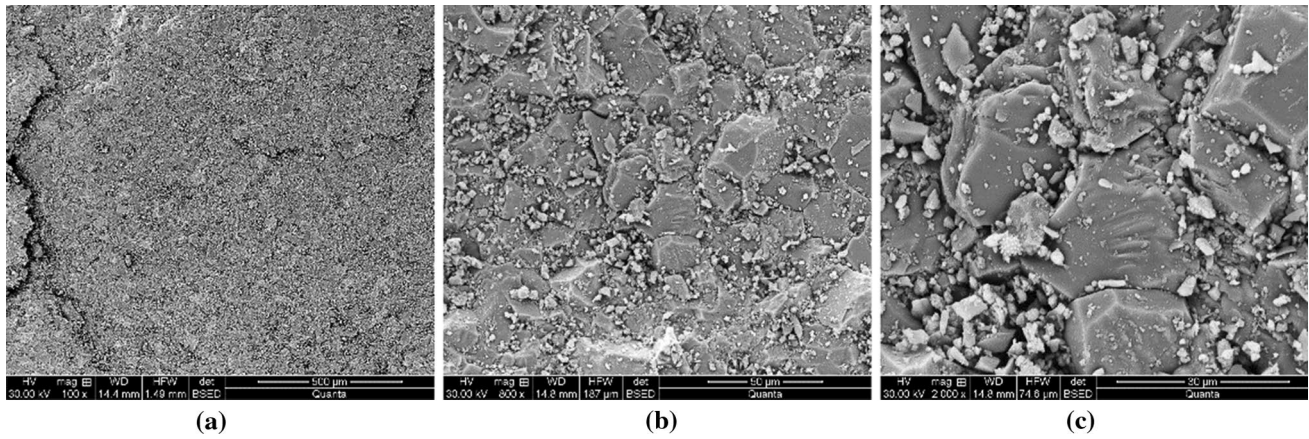


Fig. 26 Micrographs of slabs at the north-eastern sidewall inner of surrounding rock of the pilot tunnel of 7# Lab at chainage 0 + 024. **a** Magnification $\times 100$, **b** magnification $\times 800$, **c** magnification $\times 2000$

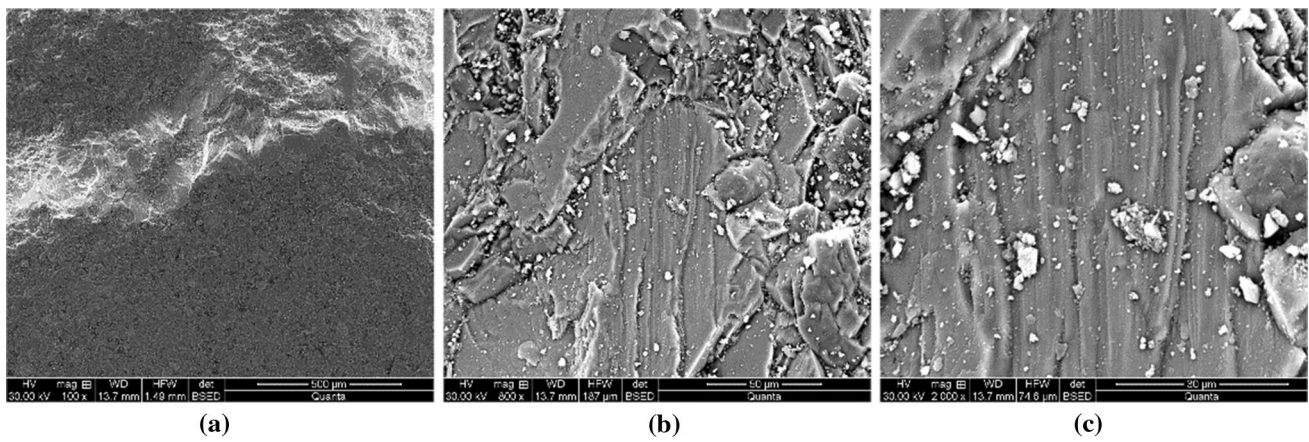


Fig. 27 Micrographs of slabs at the north-eastern floor corner of the pilot tunnel of 7# Lab at chainage 0 + 024. **a** Magnification $\times 100$, **b** magnification $\times 800$, **c** magnification $\times 2000$

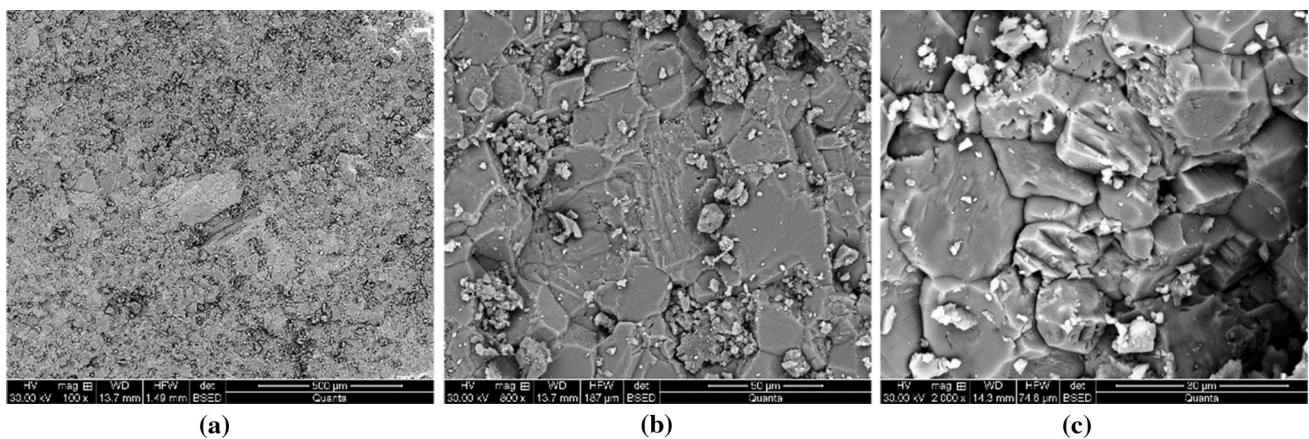


Fig. 28 Micrographs of marble samples without spalling. **a** Magnification $\times 100$, **b** magnification $\times 800$, **c** magnification $\times 2000$

Acknowledgements This work is financially supported by the National Natural Science Foundation of China under Grant Nos.11232014, 51621006, 41320104005 and 41572296. The assistances for the in situ test from Professors Shi-Yong Wu, Xiong-Hui Zeng, and Ji-Min Wang, Dr. Ya-Xun Xiao, Dr. Guang-Liang Feng, Dr. Zhi-Bin Yao, Dr. Zhao-Feng Wang and numerical simulation analysis from Dr. Yang-Yi Zhou are acknowledged.

References

- Andersson JC, Martin CD, Stille H (2009) The Äspö pillar stability experiment: part II—rock mass response to coupled excavation-induced and thermal-induced stresses. *Int J Rock Mech Min Sci* 46(5):879–895
- Cai M (2008) Influence of intermediate principal stress on rock fracturing and strength near excavation boundaries—insight from numerical modeling. *Int J Rock Mech Min Sci* 45(5):763–772
- Cheon DS, Jeon S, Chan P, Song WK, Park ES (2011) Characterization of brittle failure using physical model experiments under polyaxial stress conditions. *Int J Rock Mech Min Sci* 48(1):152–160
- Diederichs MS (2007) The 2003 Canadian geotechnical colloquium: mechanistic interpretation and practical application of damage and spalling prediction criteria for deep tunnelling. *Can Geotech J* 44(9):1082–1116
- Dowding CH, Andersson CA (1986) Potential for rock bursting and spalling in deep caverns. *Eng Geol* 22(3):265–279
- Eberhardt E (2001) Numerical modelling of three-dimension stress rotation ahead of an advancing tunnel face. *Int J Rock Mech Min Sci* 38(4):499–518
- Fairhurst C, Cook NGW (1966) The phenomenon of rock splitting parallel to the direction of maximum compression in the neighborhood of a surface. In: *Proceedings of the 1st congress of the international society of rock mechanics*, Lisbon, pp 687–692
- Feng XT (2000) *Introduction to Intelligent Rock Mechanics*. Science Press, Beijing (in Chinese)
- Feng XT, Hudson JA (2004) The ways ahead for rock engineering design methodologies. *Int J Rock Mech Min Sci* 41(2):255–273
- Feng XT, Hudson JA (2011) *Rock engineering design*. CRC Press, Boca Raton
- Feng Q, Fardin N, Jing L, Stephansson O (2003) A new method for in situ non-contact roughness measurement of large rock fracture surfaces. *Rock Mech Rock Eng* 36(1):3–25
- Feng XT, Zhang CQ, Qiu SL, Zhou H, Jiang Q, Li SJ (2013) *Dynamic design method for deep tunnels at hard rocks*. Science Press, Beijing (in Chinese)
- Feng XT, Wu SY, Li SJ, Qiu SL, Xiao YX, Feng GL, Shen MB, Zeng XH (2016) Comprehensive field monitoring of deep tunnels at Jinping underground laboratory (CJPL-II) in China. *Chin J Rock Mech Eng* 35(4):649–657 (in Chinese)
- Gwynn X (2013) Comparison of hand-mapping with remote data capture systems for effective rock mass characterisation. *Congress of the International Society for Rock Mechanics*, Lisbon
- Haneberg WC (2005) 3-D digital rock mass characterization using high-resolution photogrammetric or laser scanner point clouds. *Geol Soc Am Abstr Prog* 37(2005):245
- Haneberg WC (2007) Directional roughness profiles from threedimensional photogrammetric or laser scanner point clouds. In: Eberhardt E, Stead D, Morrison T (eds) *Rock mechanics: meeting society's challenges and demands*; proceedings of the 1st Canada–US rock mechanics symposium, Vancouver, Canada, 27–31 May 2007. Taylor and Francis, London, pp 101–106
- Hoek E, Brown ET (1980) *Underground excavation in rock*. Institute of Mining and Metallurgy, London
- Hou ZS, Gong QM, Sun SH (2011) Primary failure types and their failure mechanisms of deep buried and intact marble at Jinping II Hydropower Station. *Chin J Rock Mech Eng* 30(4):727–732 (in Chinese)
- Huang RQ, Huang D, Duan SH, Wu Q (2011) Geomechanics mechanism and characteristics of the surrounding rock mass deformation failure in construction phase for underground powerhouse of Jinping I hydropower station. *Chin J Rock Mech Eng* 30(1):23–35 (in Chinese)
- Jiang Q, Xia-Ting Feng, Guo-Qing Chen (2008) Study on constitutive model of hard rock considering surrounding rock deterioration under high geostresses. *Chin J Rock Mech Eng* 27(1):144–152
- Lan H, Martin CD, Andersson JC (2013) Evolution of in situ rock mass damage induced by mechanical-thermal loading. *Rock Mech Rock Eng* 46(1):153–168
- Li SJ, Feng XT, Wang CY, Hudson JA (2013) ISRM suggested method for rock fractures observations using a borehole digital optical televiewer. *Rock Mech Rock Eng* 46(3):635–644
- Martin CD, Christiansson R (2009) Estimating the potential for spalling around a deep nuclear waste repository in crystalline rock. *Int J Rock Mech Min Sci* 46(2):219–228
- Martin CD, Read RS (1996) AECL's mine-by experiment: a test tunnel in brittle rock. In: *Proceedings of 1st North American rock mechanics symposium (NARMS'96)*, Quebec
- Martin CD, Read RS, Martino JB (1997) Observations of brittle failure around a circular test tunnel. *Int J Rock Mech Min Sci* 34(7):1065–1073
- Ortlepp WD (1997) *Rock fracture and rock bursts: an illustrative study*. South African Institute of Mining and Metallurgy, Johannesburg, p 98
- Pate K, Haneberg WC (2011) Photogrammetric and LiDAR 3-D rock slope discontinuity mapping and interpretation surveys to improve baseline information for supporting design and construction of capital improvement projects at hydroelectric facilities. *American Rock Mechanics Association*, 520
- Pollard D, Aydin A (1988) Progress in understanding jointing over the past century. *Geol Soc Am Bull* 100:1181–1204
- Qiu SL, Feng XT, Zhang CQ, Xiang TB (2014) Estimation of rock burst wall-rock velocity invoked by slab flexure sources in deep tunnels. *Can Geotech J* 51(5):520–539
- Read RS (2004) 20 years of excavation response studies at AECL's underground research laboratory. *Int J Rock Mech Min Sci* 41(8):1251–1275
- Wu SY, Gong QM, Wang G, Hou ZS, She QR (2010) Experimental study of spalling failure for deep buried marble at Jinping II Hydropower Station and its influence on TBM excavation. *Chin J Rock Mech Eng* 29(6):1089–1095 (in Chinese)
- Wu WP, Feng XT, Zhang CQ, Qiu SL (2011) Classification of failure modes and controlling measures for surrounding rock of deep tunnel in hard rock. *Chin J Rock Mech Eng* 30(9):1782–1802 (in Chinese)
- Zhang CQ, Zhou H, Feng XT (2007) Stability assessment of rock mass engineering based on failure approach index. *Rock Soil Mech* 28(5):888–894 (in Chinese)